nature communications

Article

https://doi.org/10.1038/s41467-025-59437-3

Axial ligand induces the charge localization of Ca single-atom sites for efficient Na–S batteries

Received: 27 May 2024

Accepted: 23 April 2025

Published online: 12 May 2025

Check for updates

Fangcai Zheng[1,2,5], Yuhang Zhang[1,2,5], Zhiqiang Li[1,2], Ge Yao[1,2], Lingzhi Wei[2], Changlai Wang[3] ✉, Qianwang Chen[1,4] & Hui Wang[1] ✉

The main-group s-block metal single-atom catalysts (SACs) are typically regarded as catalytically inactive for sulfur conversion reactions in sodium–sulfur batteries. Herein, we design efficient calcium (Ca) SACs coordinated with one axial N atom and four planar O atoms (Ca-O_4N-C) for sodium–sulfur batteries. The axial N ligand induces the charge localization at Ca sites to strengthen *p-p* orbital-hybridization between Ca centers and sulfur species, which boosts the affinity toward sodium polysulfides (Na_2S_n) and simultaneously promotes the conversion kinetics. The Ca-O_4N-C@S exhibits superior sulfur conversion activity of 1211 mAh g^{-1} based on the mass of sulfur at 335 mA g^{-1} after 100 cycles under a sulfur loading of 1.0 mg cm^{-2} with an electrolyte of 2M sodium bis(trifluoromethylsulfonyl)imide in propylene carbonate/fluoroethylene carbonate and an electrolyte-to-sulfur ratio of 70 µL mg^{-1}, which is well-placed among *d*-block SACs for sodium–sulfur batteries. This work regulates the p orbital charge distribution of Ca SACs for efficient sodium–sulfur batteries.

The widespread application of portable electronics and electric vehicles has prompted extensive exploration of energy storage systems with excellent performance-to-price ratios[1,2]. Room-temperature sodium–sulfur (Na–S) batteries are considered to be one of the most promising candidates owing to their high energy density of 1274 Wh kg^{-1}, abundant sodium resources on the earth, and low cost of sulfur and sodium[3,4]. However, the detrimental shuttle effect of sodium polysulfides (Na_2S_n) and sluggish reaction kinetics result in low reversible capacity and limit the commercial application of Na–S batteries[5]. To solve these intractable issues, polar materials (e.g., metal oxides, metal carbides, metal nanoparticles) were extensively introduced into porous carbon matrix as polar active sites to improve the interaction with Na_2S_n and accelerate the reaction kinetics of polysulfides conversion, thereby promoting the performance of Na–S batteries[6–8]. Though the conversion kinetics and the anchoring ability of Na_2S_n are optimized to a certain extent, the introduction of metal compounds with a high mass percentage composition reduces the energy density of the entire battery[9,10]. Therefore, to realize high-performance Na–S batteries, it is crucial to introduce highly efficient catalysts into the carbon cathode to simultaneously enhance the adsorption ability and reaction kinetics.

Single-atom catalysts (SACs) are wildly introduced into carbon cathode for Na–S batteries owing to their high atom utilization ratio and potential catalytic activity in the conversion of Na_2S_n into the complete discharge product of Na_2S[11–13]. Generally, SACs reported so far for Na–S batteries have been focused on d-block transitional metal (M) centers with similar planar M–N_4 coordination structures, which provide empty d_{z^2} orbital to accommodate the p electrons of Na_2S_n

[1]High Magnetic Field Laboratory, Hefei Institutes of Physical Science, Chinese Academy of Sciences, Hefei, Anhui 230031, P. R. China. [2]Institutes of Physical Science and Information Technology, Key Laboratory of Structure and Functional Regulation of Hybrid Materials of Ministry of Education, Anhui University, Hefei 230601, P. R. China. [3]Graduate School of Engineering, Nagoya University, Furo-cho, Chikusa-ku, Nagoya 464-8603, Japan. [4]Hefei National Laboratory for Physical Science at Microscale and Department of Materials Science & Engineering, University of Science and Technology of China, Hefei 230026, P. R. China. [5]These authors contributed equally: Fangcai Zheng, Yuhang Zhang. ✉e-mail: wclai@ustc.edu.cn; hw39@hmfl.ac.cn

and accelerate the conversion reaction efficiency[14,15]. However, these planar M–N_4 structures with symmetrical charge distribution are not conducive for the electron transfer, and offer limited ability to strengthen the adsorption of polar Na_2S_n and improve the reaction kinetics *via* weak *d-p* orbital-hybridization between SACs and Na_2S_n[16–19]. To today, regulating the coordination environment is wildly confirmed as an effective strategy for deliberately adjusting the *d* electron distribution on SACs centers for Na–S batteries[20–23]. For example, our group ever demonstrated that Zn–N_2 SACs were favorable for boosting the conversion of sulfur species in Na–S batteries in comparison with Zn–N_4 SACs[24]. Zhang et al. also confirmed that the unsaturated Fe–N_2 single-atom structure facilitated to the adsorption of polysulfides and accelerated the sulfur conversion kinetics[25]. These results demonstrate that regulating the coordination environment could be an effective pathway to boost the catalytic activity of SACs for Na–S batteries.

In contrast to d-block transitional metals, *s*-block main-group metals lacking valence electrons show an unsatisfactory ability to activate sulfur species conversion in Na–S batteries[26–28]. In this context, *s*-block main-group metals are rarely investigated to optimize the sulfur conversion electrochemistry in Na–S batteries. However, recent researches have demonstrated that the *p* electrons in *s*-block metals can be further activated through breaking the symmetry of main-group single-atom center, thereby displaying promising catalytic activity via the optimized overlap between the *p* orbitals of *s*-block metals and reaction intermediates[29]. For example, our group ever regulated the *p*-orbital electron structure of Ca through the construction of N,O-coordinated asymmetrical single-atom center to optimize the interaction with the reaction intermediates of oxygen species and then boost the catalytic activity for the ORR[30]. Liu et al. designed planar Ca-N_3O single-atom structures to induce the electron localization on *p*-orbitals at Ca sites, thus boosting the catalytic activity of CO_2 electroreduction to CO[31]. Therefore, it is feasibly deduced that breaking the symmetry of metal single-atom structure can induce the localized p orbital charge distribution on *s*-block metal center as an active site for Na–S batteries.

Herein, we successfully designed a facile strategy to construct *s*-block Ca SACs supported on nitrogen-doped carbon materials for Na–S batteries, in which the p orbital electron distribution of Ca sites was precisely regulated by the introduction of axial N ligands. The atomically dispersed Ca single-atom sites effectively confine the shuttle diffusion of soluble Na_2S_n and provide abundant catalytic sites to accelerate the reaction kinetics for Na–S batteries. Interestingly, X-ray adsorption fine structure (XAFS) results demonstrate that the axial O atom in the oversaturated Ca–O_5 coordination structure (Ca-O_5-C) can be substituted by an N atom (Ca-O_4N-C) via the thermal NH_3 etching. The density functional theory (DFT) results combined with electrochemical measurements confirm that the introduction of axial N atom can result in more localized *p* orbital charge on Ca single-atom sites in Ca–O_4N configuration than that in Ca–O_5 configuration, which enhances the affinity for Na_2S_n and simultaneously promotes the conversion kinetics of Na–S batteries owing to the strengthened *p-p* orbital-hybridization between Ca SACs and sulfur species. This work offers a facile strategy to precisely regulate the highly active Ca–O_4N configuration for the potential application in advanced Na–S batteries.

Results

Synthesis and structural characterizations

Figure 1a displays the synthesis procedure of Ca-O_4N-C, and the synthetic details are described in the experimental section. Ca-based metal-organic frameworks (Ca-BTC) constituted by Ca^{2+} and trimesic acid were first applied as a precursor for the synthesis of Ca-O_4N-C. As shown in Supplementary Fig. 1, Ca-BTC exhibits a sheet-like morphology. The thermal decomposition temperature of Ca-BTC under N_2 was investigated by thermogravimetric analysis (TGA) (Supplementary Fig. 2). After the pyrolysis process, the Ca–O clusters in the Ca-BTC were transformed into ultrafine $CaCO_3$ nanocrystals embedded into in situ generated carbon skeleton (Supplementary Fig. 3). X-ray diffraction (XRD) pattern (Supplementary Fig. 4) confirms that $CaCO_3$ nanocrystals are easily removed by an acid etching process, and then Ca-O_5-C is successfully obtained. The scanning electron microscopy (SEM) and transmission electron microscopy (TEM) results (Fig. 1b and Supplementary Fig. 5) exhibit that Ca-O_5-C still retains a sheet-like morphology without any nanoparticles. The high-angle annular dark-field scanning transmission electron microscopy (HAADF–STEM) image (Fig. 1c) confirms the existence of abundant bright dots on the carbon skeleton, which can be attributed to Ca single atoms. Besides, the element mapping (Fig. 1d) of Ca-O_5-C also verifies the existence of Ca single atoms.

In contrast to Ca-O_5-C, no new phase is formed in the XRD pattern of Ca-O_4N-C, and two broad peaks confirm the formation of disordered carbon with low crystallinity (Supplementary Fig. 6). In addition, the Ca-O_4N-C maintains a similar morphology to Ca-O_5-C, and large number of atomically dispersed bright dots are also observed in Ca-O_4N-C (Fig. 1e, f and Supplementary Fig. 7). Nevertheless, the element mapping (Fig. 1g) confirms the existence of N atoms in Ca-O_4N-C. Raman results confirm that the I_D/I_G ratio of Ca-O_4N-C (0.955) is higher than that of Ca-O_5-C (0.938), demonstrating that the thermal NH_3 etching can remove some edge–O groups and increase the density of defective structure in carbon materials (Supplementary Fig. 8)[32]. Compared with that of Ca-O_5-C, containing distinctive peaks of C and O, the X-ray photoelectron spectrum (XPS) survey spectrum of Ca-O_4N-C has a new peak of N (Supplementary Figs. 9, 10), confirming the successful introduction of N atom in Ca-O_4N-C. Besides, the elemental analysis shows that the ratio of N in Ca-O_4N-C is 3.25 wt%. The absence of the Ca peak in the XPS survey demonstrates the low Ca content in Ca-O_4N-C and Ca-O_5-C. The inductively coupled plasma optical emission spectroscopy (ICP-OES) further confirms that the contents of Ca atom in Ca-O_5-C and Ca-O_4N-C are 1.22 and 1.56 wt%, respectively. The relatively high Ca loading in Ca-O_4N-C originates from the removal of unstable groups by the thermal NH_3 etching.

The details of coordinated environments of Ca-O_5-C and Ca-O_4N-C were further confirmed by X-ray adsorption near-edge structure (XANES) and extended X-ray adsorption fine structure (EXAFS) spectroscopies. As shown carbon K-edge in Fig. 2a, both Ca-O_5-C and Ca-O_4N-C display typical adsorption peaks at 286 and 293 eV, which corresponds to graphitic C–C π* and graphitic C–C σ* resonances of carbon materials[33], respectively. Moreover, the weak peak at about 289 eV corresponds to C–O–C and C–N–C configurations[34]. As shown in Fig. 2b, in comparison with the standard N-doped graphene, the nitrogen K-edge curves display that pyridinic-N and pyrrolic-N exist in Ca-O_4N-C. Besides, the oxygen K-edge curves (Fig. 2c) show that both Ca-O_5-C and Ca-O_4N-C contain C=O π* and C–O σ* resonances[35]. To further confirm the coordinated fine structure of Ca centers in Ca-O_5-C and Ca-O_4N-C, the Ca K-edge XANES of Ca-O_5-C and Ca-O_4N-C is close to CaO (Fig. 2d), suggesting that Ca atoms serve as oxidation state in Ca-O_5-C and Ca-O_4N-C. Besides, as shown in the inset of Fig. 2d, the white line of Ca-O_4N-C shifts negatively in contrast to that of Ca-O_5-C, which probably due to that one of O atoms in Ca-O_5-C is substituted by an N atom[36]. As shown in Fig. 2e, the Fourier transformation EXAFS spectra show the atomically dispersed Ca atoms in Ca-O_5-C and Ca-O_4N-C. The fitting results (Fig. 2f, g and Supplementary Table 1) demonstrate that the coordination number of Ca in Ca-O_5-C is about 5, while after the O atom substituted by an N atom, the coordination number of Ca in Ca-O_4N-C is still close to 5. Moreover, the length (2.241 Å) of the axial Ca–O bond is different with that of the other four planar Ca–O bonds (2.389 Å) in Ca-O_5-C, while the length of four Ca–O bonds (2.370 Å) is same in Ca-O_4N-C, suggesting the axial O atom in Ca-O_5-C is substituted by an N atom. Besides, the calculation results confirm that the bond lengths of Ca–O and Ca–N in Ca-O_5-C and Ca-

https://doi.org/10.1038/s41467-025-59437-3

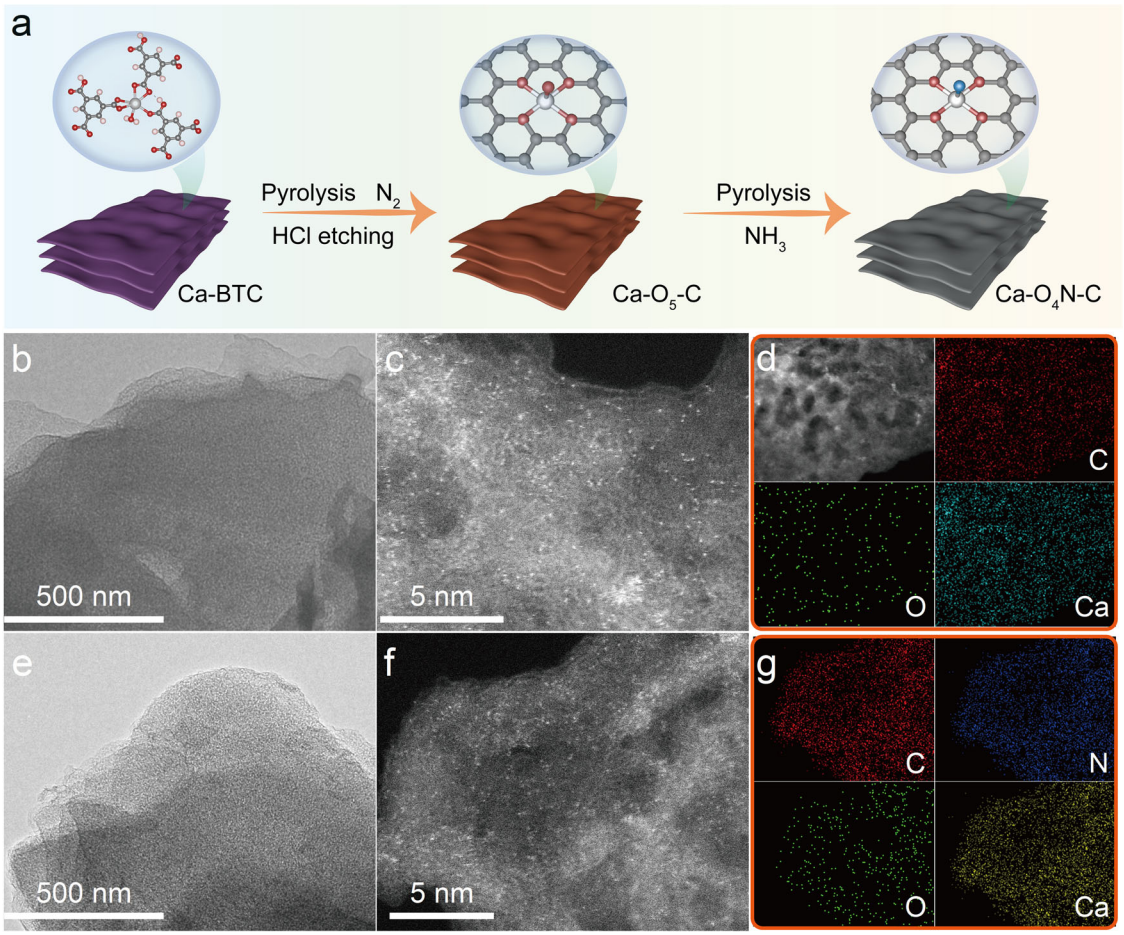

Fig. 1 | Schematic illustration and morphology characterization. a The illustration of the fabrication process of Ca-O_4N-C. **b** TEM image of Ca-O_4N-C. **c** HAADF–STEM image of Ca-O_4N-C. **d** Elemental maps of Ca-O_5-C. **e** TEM image of Ca-O_5-C. **f** HAADF–STEM image of Ca-O_5-C. **g** Elemental maps of Ca-O_4N-C.

O_4N-C are consistent with the calculated values in the models of Ca–O_5 and Ca–O_4N (Supplementary Fig. 11), which further verifies the fitting results of EXAFS spectra. Wavelet transform (WT) of Ca K-edge EXAFS data were further conducted (Fig. 2h, i), and the results revealed the coordination environment of Ca–O_4N-C was different with that of Ca–O_5-C. From the above analysis, it can be confirmed that the N atom acts as the axial Ca–N bond in Ca–O_4N-C.

The N_2 adsorption/desorption isotherms were measured by Brunauer–Emmett–Teller (BET) (Supplementary Figs 12,13 and Supplementary Table 2). The Ca-O_4N-C displays a specific surface area of 1147 $m^2 g^{-1}$ and a pore volume of 1.810 $cm^3 g^{-1}$. Those values are 1035 $m^2 g^{-1}$ and 1.618 $cm^3 g^{-1}$ for Ca-O_5-C. The enhanced specific surface area and pore volume further confirm that the thermal NH_3 etching can introduce the defective structure in Ca-O_4N-C, which further supports the Raman results. Besides, Ca-O_5-C and Ca-O_4N-C show a similar pore size distribution centered at 0.5–1.0 nm and 3–5.0 nm, demonstrating the coexistence of micro- and mesopores. The large pore volume can provide an interconnected internal space to accommodate sulfur and accelerate the ion transport[20]. Owing to the high thermal stability of Ca-O_5-C and Ca-O_4N-C (Supplementary Fig. 14), a molten diffusion approach was used to load sulfur. Nevertheless, after the infiltration of sulfur, the specific surface areas of Ca-O_4N-C@S and Ca-O_5-C@S decrease significantly to 172 and 101 $m^2 g^{-1}$, respectively, and their pore volumes also drop sharply to 0.506 and 0.415 $cm^3 g^{-1}$, respectively. Moreover, the reduction of pore size can also be observed in Ca-O_4N-C@S and Ca-O_5-C@S. This confirms the impregnation of sulfur into the pore structure of Ca-O_4N-C and Ca-O_5-C. Besides, TGA results (Supplementary Fig. 15) show that the sulfur loading mass is 55.2 and 53.2 wt% for Ca-O_4N-C@S and Ca-O_5-C@S, respectively. As a comparison, nitrogen-doped carbon materials (NCs) without Ca catalytic centers were also synthesized to confirm the promotion effect of Ca SACs on the conversion of Na_2S_n into the product of Na_2S. The morphology and XRD pattern of the resulting NCs is similar with Ca-O_4N-C and Ca-O_5-C (Supplementary Figs. 16, 17). Moreover, the XRD patterns of Ca-O_4N-C@S, Ca-O_5-C@S, and NCs@S display unobvious diffraction peaks for sulfur (Supplementary Fig. 18). Raman spectra also confirm the absence of sulfur peaks (Supplementary Fig.19). These results demonstrate the successful melting of sulfur into their pore structures. In contrast, NCs@S has a low sulfur loading mass of 51.8 wt%. The higher loading mass of sulfur in Ca-O_4N-C@S can be probably attributed to the strong affinity toward S_8 molecules caused by the enhanced specific surface area and pore volume[20,37]. In addition, as shown in Supplementary Fig. 20, it is clearly observed that sulfur is well dispersed in the skeleton of Ca-O_4N-C, where the atomically dispersed Ca catalytic centers are beneficial for the fast adsorption of the timely generated Na_2S_n and thus accelerate the sulfur conversion kinetics.

To verify the structural advantage of Ca–O_4N configuration in the catalytic conversion of Na_2S_n into Na_2S, the Na_2S_n adsorption test was first explored. Ca-O_4N-C and Ca-O_5-C were immersed into Na_2S_6 solution, and as shown in Fig. 3a, the solution with Ca-O_4N-C became colorless, while the one with Ca-O_5-C exhibited pale yellow, demonstrating the stronger adsorption capability of Ca-O_4N-C toward Na_2S_6. Nevertheless, the solution with NCs still remained yellow. Besides, UV–vis adsorption spectra (Fig. 3a and Supplementary Fig. 21) confirm that Ca-O_4N-C owns the faster adsorption rate toward Na_2S_6.

https://doi.org/10.1038/s41467-025-59437-3

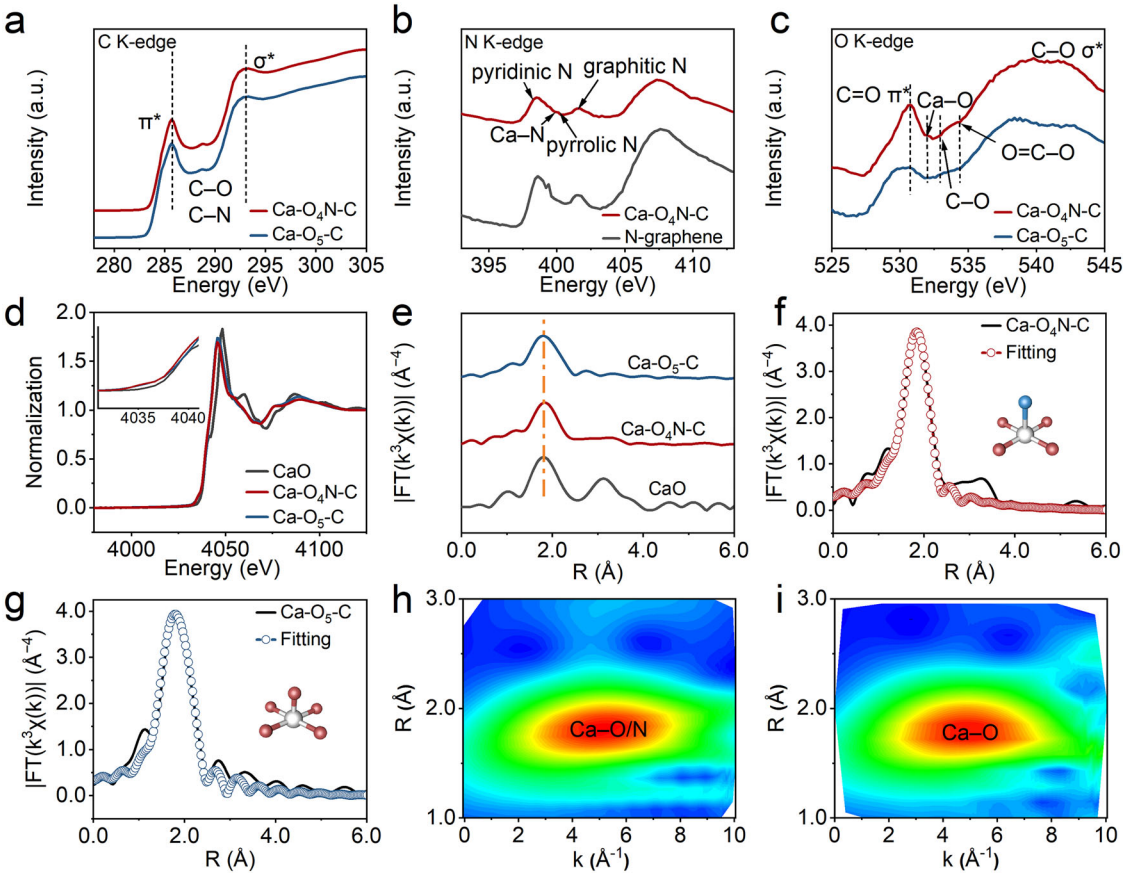

Fig. 2 | Structural characterizations. a C K-edge XANES spectra of Ca-O_4N-C and Ca-O_5-C. **b** N K-edge XANES spectra of Ca-O_4N-C and N-graphene. **c** O K-edge XANES spectra of Ca-O_4N-C and Ca-O_5-C. **d** XANES results of Ca K-edge and **e** Fourier transforms of Ca K-edge EXAFS spectra of Ca-O_4N-C, Ca-O_5-C, and CaO. EXAFS fitting curves in R-space of **f** Ca-O_4N-C and **g** Ca-O_5-C. WT plots of **h** Ca-O_4N-C and **i** Ca-O_5-C.

As shown in Fig. 3b and Supplementary Fig. 22, XPS tests also demonstrate that the electron is more easily transferred from Na_2S_6 to Ca-O_4N-C in comparison with Ca-O_5-C[24,38]. Besides, DFT calculation was also performed to investigate the electron transfer between Na_2S_6 and the catalysts. About 0.0498 electron is transferred from Na_2S_6 to the Ca–O_4N center, while 0.0388 electron is transferred from Na_2S_6 to the Ca–O_5 center (Fig. 3c), suggesting the superior affinity of Ca-O_4N-C toward Na_2S_6. The symmetric cell was assembled to investigate the Na_2S_n conversion kinetics, and the cyclic voltammogram (CV) curves based on Ca-O_4N-C, Ca-O_5-C and NCs are shown in Supplementary Fig. 23. The Ca-O_4N-C exhibits the higher current response than those of Ca-O_5-C and NCs, demonstrating the remarkable catalytic activity of the Ca–O_4N centers for Na_2S_n conversion. The Na_2S nucleation was also conducted to explore the superior catalytic activity of Ca-O_4N-C toward the conversion of Na_2S_n into Na_2S. As shown in Fig. 3d–f and the corresponding enlarged inset, Ca-O_4N-C displays higher and earlier current response (0.30 mA at 2561 s for Ca-O_4N-C, 0.21 mA at 4465 s for Ca-O_5-C, and 0.03 mA at 6848 s for NCs). Besides, the capacity of Na_2S nucleation (598 mAh g^{-1}) on Ca-O_4N-C is also higher than those of Ca-O_5-C (443 mAh g^{-1}) and NCs (75 mAh g^{-1}). These results demonstrate that Ca-O_4N-C effectively accelerates the reaction kinetics of Na_2S_n conversion[39].

Electrochemical performance of Na–S batteries

The electrochemical performance of Ca-O_4N-C@S was further investigated for Na–S batteries. The first CV curve of Ca-O_4N-C@S was measured at 0.1 mV s^{-1} (Supplementary Fig. 24). The cathodic peaks at 1.95 and 0.83 V can be attributed to the conversion of S to long-chain Na_2S_n ($4<n\leq 8$) and the formation of Na_2S_2/Na_2S[14], respectively. A strong anodic peak at 2.06 V represents the conversion of short-chain Na_2S_n to long-chain Na_2S_n[20]. Fig. 3g shows the second CV curve of Ca-O_4N-C@S, and two clear cathodic peaks at 1.58 and 1.10 V is indexed to the conversion of Na_2S_n ($4\leq n\leq 8$) into Na_2S_4 and then into Na_2S_2/Na_2S[40]. The oxidation peak at 2.01 V corresponds to the reversible conversion of Na_2S_2/Na_2S into S_8 molecules[41,42]. The second CV curves of Ca-O_5-C@S and NCs@S were also investigated, and the intensity of redox peaks decreases in the order of Ca-O_4N-C@S, Ca-O_5-C@S, and NCs@S. Besides, compared with Ca-O_5-C@S and NCs@S, the reduction peak of Ca-O_4N-C@S shifts positively, while its oxidation peak shifts negatively. Compared with Ca-O_5-C@S (443/324 mV dec^{-1}) and NCs@S (567/293 mV dec^{-1}), Ca-O_4N-C@S exhibits lower Tafel slopes of 229 and 276 mV dec^{-1} for the reduction and oxidation processes (Fig. 3h, i), respectively, which reveals that the active Ca sites in Ca–O_4N configuration facilitate the Na_2S_n conversion in Na–S batteries[32].

Figure 4a displays the cycling performances of Ca-O_4N-C@S, Ca-O_5-C@S and NCs@S at 0.2 C (335 mA g^{-1}, 1.0 C = 1675 mA g^{-1}). A higher capacity of 1211 mAh g^{-1} is still maintained for Ca-O_4N-C@S compared to Ca-O_5-C@S (1014 mAh g^{-1}) and NCs@S (635 mAh g^{-1}) after 100 cycles. Besides, the electrode with an active mass loading of 80% still retains a capacity of 1109 mAh g^{-1} at 0.2 C after 100 cycles (Supplementary Fig. 25). When the mass loading was increased up to 3.78 mg cm^{-2}, it still displayed a capacity of 978 mAh g^{-1} at 0.2 C after 100 cycles (Supplementary Fig. 26). Fig. 4b exhibits the second galvanostatic charge/discharge (GCD) curves of Ca-O_4N-C@S, Ca-O_5-C@S, and NCs@S at 0.2 C. Ca-O_4N-C@S exhibits a smaller discharge/charge potential gap of 0.71 V than Ca-O_5-C@S (0.74 V) and NCs@S (0.79 V), suggesting that Ca–O_4N single-atom center can promote the sulfur

https://doi.org/10.1038/s41467-025-59437-3

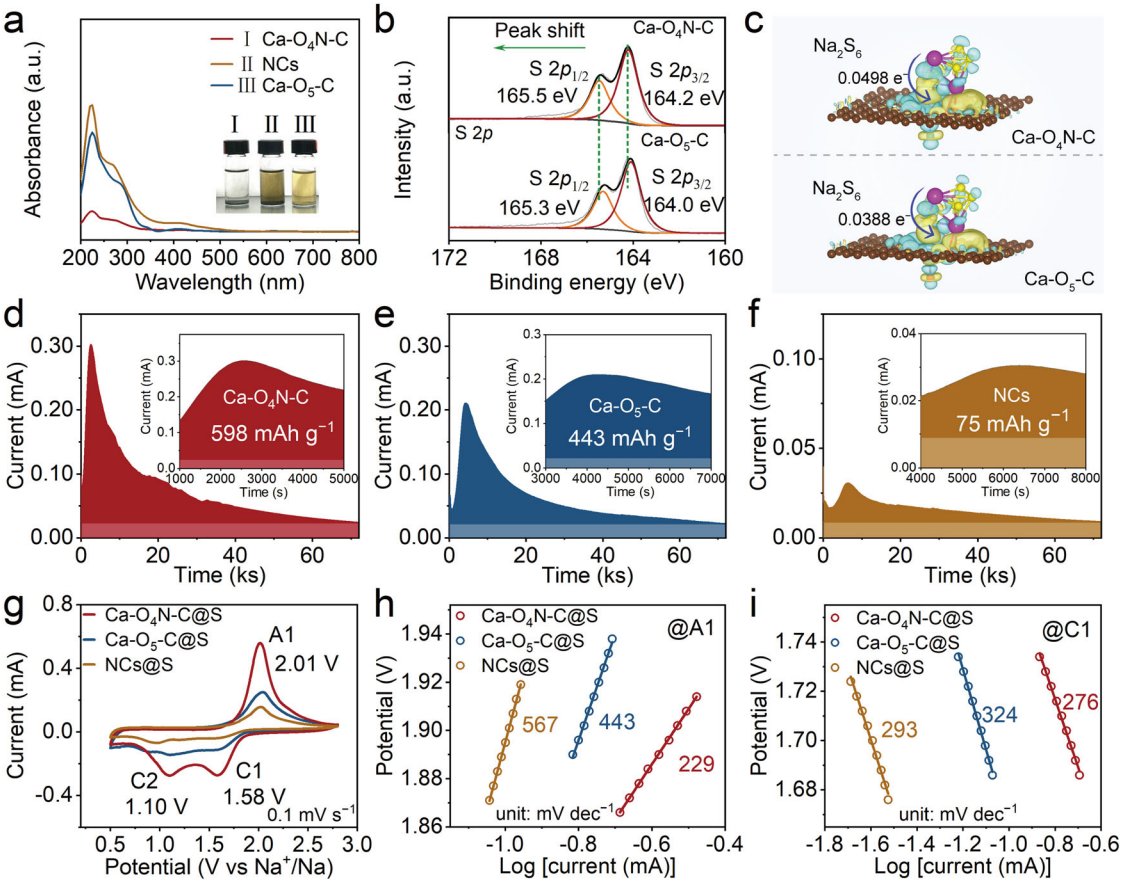

Fig. 3 | Electrochemical adsorption and catalytic mechanism. a UV/vis spectra and digital photo of Na_2S_6 solution before and after adsorbed by Ca-O_4N-C, Ca-O_5C and NCs. **b** The S 2*p* spectra of Na_2S_6 adsorbed in Ca-O_4N-C and Ca-O_5C. **c** The diagrams of charge density difference for Na_2S_6 adsorbed on the Ca-O_4N-C and Ca-O_5C models. **d**–**f** Potentiostatic discharge curves of Na_2S_6 on Ca-O_4N-C, Ca-O_5-C and NCs. **g** CV curves of Ca-O_4N-C@S, Ca-O_5-C@S and NCs@S. **h**, **i** Tafel plots of Ca-O_4N-C, Ca-O_5-C, and NCs, which were calculated from CV curves.

reaction kinetics in Na–S batteries[43]. Besides, there are two discharge plateaus and one charge plateau in the first GCD profiles of Ca-O_5-C@S (Supplementary Fig. 27), which is consistent with the observation of the first CV curves. Figure 4c displays the rate capability, and Ca-O_4N-C@S exhibits superior rate capacities of 1316, 1240, 1144, 1036, 942, 859, and 714 mAh g^{-1} at 0.1, 0.2, 0.5, 1.0, 2.0, 3.0, and 5.0 C, respectively, which are higher than Ca-O_5-C@S and NCs@S at each current density. Besides, the capacity of Ca-O_4N-C@S can come back to the original level, and the GCD curves (Fig. 4d) still show obvious reduction/oxidation plateaus at different current rates, suggesting the good reversibility of the sulfur chemistry for Na–S batteries. In addition, Ca-O_4N-C@S also shows long cyclic stability with a capacity of 887 mAh g^{-1} after 800 cycles at 3.0 C (Fig. 4e), which is superior to that of Ca-O_5-C@S (402 mAh g^{-1}) and NCs@S (163 mAh g^{-1}). The capacity decay of Ca-O_4N-C@S is 0.017% per cycle. As shown in Supplementary Fig. 28, Ca-O_4N-C@S shows superior or even better electrochemical performance for Na–S batteries in comparison with the reported sulfur cathodes[7,17,32,41,44–48]. More importantly, the outstanding performance of Ca-O_4N-C@S was further evaluated by a pouch cell (8 × 6.5 cm^2), and a high capacity of 515 mAh g^{-1} and a Coulomb efficiency of 99.50% were observed after 50 cycles at 0.1 C (Supplementary Fig. 29). The superior sulfur conversion electrochemistry for Na–S batteries is attributed to the unique Ca–O_4N catalytic centers, which enhances the affinity toward sulfur species and accelerates the sulfur conversion kinetics.

The sulfur conversion mechanism in Na–S batteries

CV curves obtained at different scan rates were measured to explore the accelerated sulfur conversion kinetics (Supplementary Figs. 30–32). It is clearly found that the current densities of the cathode peaks and anode peaks for Ca-O_4N-C@S, Ca-O_5-C@S, and NCs@S are linear with the square roots of scan rates, suggesting a diffusion-limited process. Besides, the slopes of the reductive peak and oxidative peak for Ca-O_4N-C@S are 0.69 and 0.93, which is higher than those of Ca-O_5-C@S (0.67 and 0.89) and NCs@S (0.61 and 0.89), further confirming that Ca–O_4N single-atom center can promote the sulfur convention kinetics. The galvanostatic intermittent titration technique (GITT) was performed to investigated Na^+ diffusion coefficient (D_{Na^+}) of Ca-O_4N-C@S, Ca-O_5-C@S, and NCs@S (Fig. 5a and Supplementary Fig. 33). Obviously, the D_{Na^+} value of Ca-O_4N-C@S is higher than those of Ca-O_5-C@S and NCs@S, revealing that the Ca–O_4N single-atom center accelerates the Na^+ diffusion rate in Ca-O_4N-C@S[21,24]. As shown in Fig. 5b and Supplementary Table 3, Ca-O_4N-C@S has a smaller charge-transfer (R_{ct}) value (588 Ω) than those of Ca-O_5-C@S (620 Ω) and NCs@S (925 Ω). These results demonstrate that Ca–O_4N single-atom center displays enhanced Na^+ diffusion rate and electron transfer, leading to enhanced electrochemical performance.

To further explore the sulfur conversion mechanism, the discharge/charge process of Ca-O_4N-C@S was explored by in situ XRD. S_8 molecules was first reduced into long-chain Na_2S_n ($4 \le x \le 8$), and then the weak peaks of Na_2S_4 were presented (Fig. 5c)[24,32]. Eventually, the weak peaks of Na_2S are observed, indicating the full catalytic conversion of sulfur species to Na_2S[46]. In the charge process, Na_2S was gradually converted into Na_2S_4 and then into long-chain Na_2S_n. Finally, Na_2S_n was transformed to S_8 molecules completely[49]. Besides, the presence of a weakly reversible peak near 27° can be attributed to the peak of sulfur, which can further confirm that the Ca single-atom sites

https://doi.org/10.1038/s41467-025-59437-3

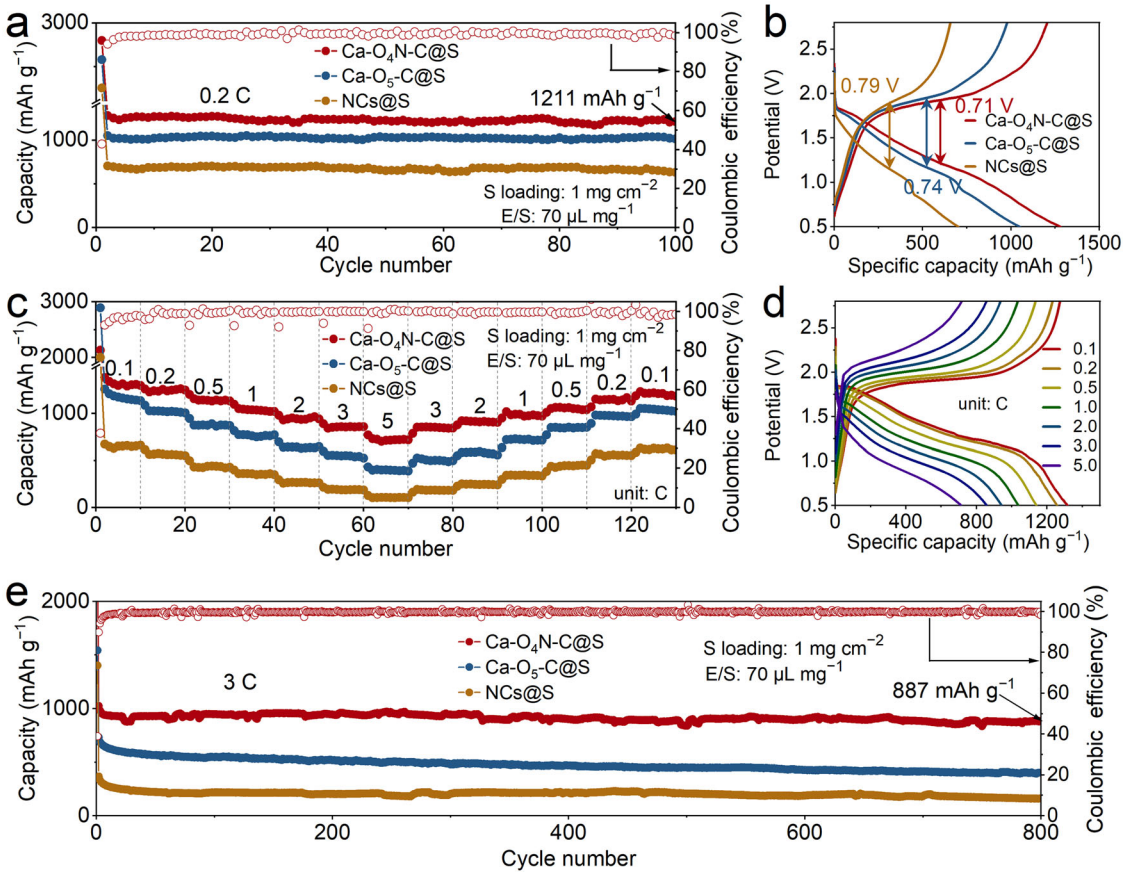

Fig. 4 | Na–S battery test. a Cycling performances, **b** GCD profiles, and **c** rate performances of Ca-O_4N-C@S, Ca-O_5-C@S and NCs@S. **d** GCD profiles of Ca-O_4N-C@S from 0.1 to 5.0 C. **e** Long cyclic performance of Ca-O_4N-C@S, Ca-O_5-C@S and NCs@S at 3 C.

can catalyze the reversible conversion of sulfur during the redox process. The sulfur conversion steps were further investigated by the ex-situ XPS, and the S 2*p* spectra showed that sulfur was initially transformed into Na_2S_n ($4 \le x \le 8$), and then into Na_2S_2 and Na_2S (Fig. 5d, e)[50]. When charged from 0.5 to 2.8 V, Na_2S and Na_2S_2 were converted into sulfur, demonstrating reversible Na–S electrochemistry (Fig. 5e)[51]. In addition, Ca-O_4N-C@S still retained an intact sheet-like morphology after cycling, and sulfur was uniformly loaded in Ca-O_4N-C, implying its high structure stability for sulfur redox reactions (Fig. 5f and Supplementary Fig. 34). Besides, XPS results (Supplementary Fig. 35) confirm the formation of NaF and Na_2CO_3 at cathode electrolyte interphase (CEI) layer, which improves the ionic conductivity and reduces the sulfur loss from the interfacial side reactions[52]. The catalytic conversion of sulfur species by Ca-O_4N-C is illustrated in Fig. 5g. The Ca–O_4N catalytic center boosts the affinity toward Na_2S_n, which effectively avoids the diffusion of soluble polysulfides and lowers the sulfur redox kinetics, endowing Ca-O_4N-C@S with long-life cycling stability.

Discussion

DFT calculation was also performed to reveal the catalytic activity of Ca SACs for the sulfur species conversion in Na-S batteries. Based on the above XAFS analysis, two kinds of Ca SACs structural models were constructed, including an axial O-coordinated Ca-O_5-C and an axial N-coordinated Ca-O_4N-C (Supplementary Figs. 36, 37). To demonstrate the thermal stability of Ca-O_5-C and Ca-O_4N-C, ab initio molecular dynamics (AIMD) simulations were first conducted. The AIMD results showed the energy oscillates near the initial value, and the structures of Ca-O_5-C and Ca-O_4N-C remained well-preserved after 10,000 fs at 300 K (Supplementary Figs. 38, 39), confirming their excellent structural stability. For comparison, the model of nitrogen-doped carbon materials (NCs) was also constructed (Supplementary Fig. 40). In the discharge process, S_8 ring molecules firstly react with two Na^+ to form long-chain Na_2S_8, which then undergoes further reduction to form Na_2S_6, Na_2S_4, Na_2S_2, and finally transforms into Na_2S. The adsorption behaviors of intermediates on Ca-O_5-C, Ca-O_4N-C, and NCs were investigated by DFT calculations. The calculated adsorption energies are displayed Fig. 6a and Supplementary Table 4, and corresponding interaction configurations are depicted in Fig. 6b and Supplementary Fig. 41. The adsorption energies of Na_2S_n on Ca-SACs are higher than those on NCs, which is attributed to the formation of Ca–S bonds between Ca SACs and Na_2S_n, effectively trapping Na_2S_n intermediates and inhibiting the shuttle effect[53,54]. Interestingly, the adsorption strength of Na_2S_n species on Ca-O_4N-C is stronger than that on Ca-O_5-C, suggesting that Ca-O_4N-C has a stronger affinity capability toward Na_2S_n species (Supplementary Table 4). Subsequently, the reaction pathways of the sulfur reduction reaction on Ca SACs and NCs were calculated. As displayed in Gibbs free energy (ΔG) profiles (Fig. 6b and Supplementary Fig. 41), the transformation of the S_8 ring molecule into Na_2S_8 and Na_2S_6 on Ca SACs and NCs is relatively straightforward as these steps are exothermic; however, the following conversion of long-chain Na_2S_6 into shorter-chain Na_2S_4, Na_2S_2, and Na_2S are quite sluggish. For NCs, the transformation of Na_2S_2 into Na_2S is the most difficult step with a large energy barrier of 0.77 eV (Supplementary Fig. 41). The transformation of Na_2S_4 into Na_2S_2 on Ca SACs is the rate-limiting step, and compared with Ca-O_5-C (Fig. 6b), the Ca-O_4N-C could facilitate the sluggish kinetics of sulfur reduction in discharge process as it has a lower the energy barrier.

During the charging process, Na_2S will be oxidized back to the charged product. The decomposition energy barriers of Na_2S on

https://doi.org/10.1038/s41467-025-59437-3

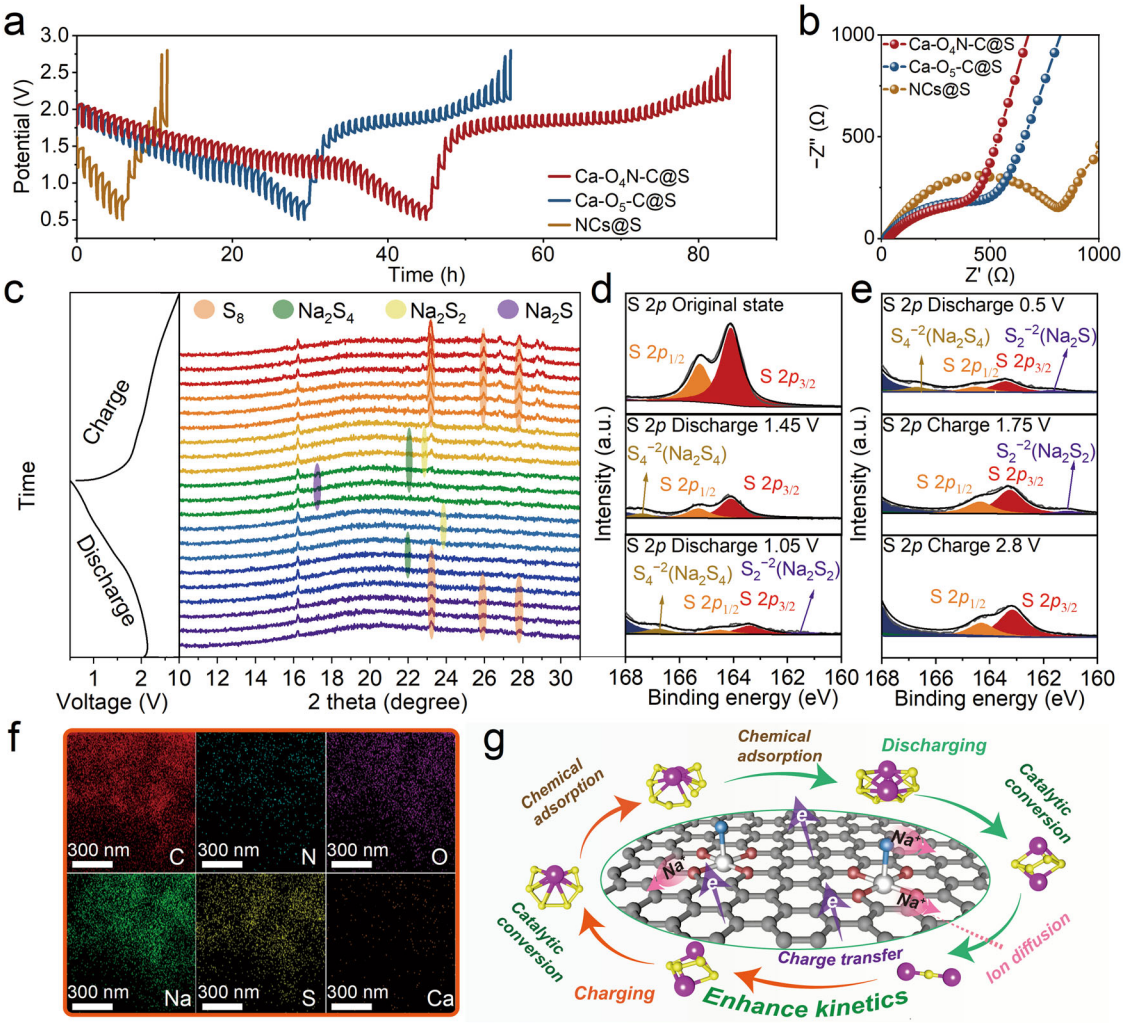

Fig. 5 | Characterizations of mechanism. a GITT curves and **b** Nyquist plots of Ca-O_4N-C@S, Ca-O_5-C@S, and NCs@S. **c** In situ XRD patterns and **d**, **e** ex-situ XPS spectra of Ca-O_4N-C@S. **f** Elemental maps of Ca-O_4N-C@S after cycling. **g** Schematic of catalytic conversion of sulfur species by Ca-O_4N-C.

Ca-O_5-C and Ca-O_4N-C were calculated using the climbing-image nudged elastic band (CI–NEB) method[55]. The dissociation processes begin from the initial state (IS) of Na_2S to the final state (FS) of NaS cluster and a single Na ion ($Na_2S \rightarrow NaS + Na^+ + e^-$) via a transition state (TS). The energy profiles for the Na_2S decomposition processes on Ca-O_5-C and Ca-O_4N-C are presented in Fig. 6c, d. The calculated results show that the Na_2S decomposition processes on Ca SACs are endothermic. The activation energy of Na_2S decomposition on Ca-O_5-C (1.64 eV) is higher than that on Ca-O_4N-C (1.59 eV). Therefore, Ca-O_4N-C could accelerate the catalytic oxidation of Na_2S by decreasing the activation energy in the charging process. To assess the effectiveness of Ca-O_5-C and Ca-O_4N-C in preventing "catalyst poisoning", the binding energies of the Ca-O_5-C and Ca-O_4N-C with isolate sulfur atom were calculated[56]. The optimal geometrical configurations and the corresponding binding energies for Ca-O_5-C and Ca-O_4N-C with adsorbed isolate sulfur atom are presented in Supplementary Figs. 42, 43 and Supplementary Table 5, respectively. According to the data in Supplementary Table 5, both Ca-O_5-C (−1.67 eV) and Ca-O_4N-C (−2.21 eV) exhibit moderate binding energies with sulfur, indicating Ca-O_5-C and Ca-O_4N-C possess moderate Ca–S interactions. The moderate Ca–S interactions enable Ca-O_5-C and Ca-O_4N-C to dissociate from the Ca–S bond during the charge-discharge cycles, effectively preserving their active catalytic sites, which facilitate balanced and efficient bidirectional catalytic functions, thereby improving the reversibility of Na–S batteries[57].

To explore the superiority of Ca-O_4N-C@S for Na–S batteries, the electronic structures of Ca-O_5-C and Ca-O_4N-C were further calculated. The *p* band center of Ca in Ca-O_5-C and Ca-O_4N-C were calculated. The partial density of states (PDOS) shows that the Ca-3*p* orbitals of Ca SACs are very localized. Compared to the *p* band center of Ca in Ca-O_4N-C (−2.38 eV), the p band center of Ca in Ca-O_5-C (−7.64 eV) shifted down (Supplementary Fig. 44), which was attributed to the stronger electronegativity of O than N. This difference in electronegativity causes electrons to transfer from Ca to the surrounding O and N atoms. This charge transfer is clearly observed in Fig. 6e, f, and the electron distribution of the Ca-O_4N-C is more localized around the Ca atom compared to Ca-O_5-C. The downshift of the Ca *p* band center resulted in a weaker adsorption strength of Na_2S_n on Ca-O_5-C than on Ca-O_4N-C.

To further understand the bonding between Na_2S_6 and Ca SACs, the projected crystal orbital Hamilton population (pCOHP) were calculated to understand the bonding between Na_2S_6 and Ca SACs[58–60]. As shown in Fig. 6g, there is a strong *p*-*p* orbital-hybridization between Ca atom and sulfur atom, forming bonding orbitals and antibonding orbitals. The valence states were mainly composed of bonding orbitals, while the antibonding orbitals were mainly located in the conduction band. However, there were also a small number of antibonding orbitals in the valence band. To gain deeper quantitative insights, the integrated COHP (ICOHP) was determined by integrating the energy up to the highest occupied bands (below E_F). The integrated pCOHP values

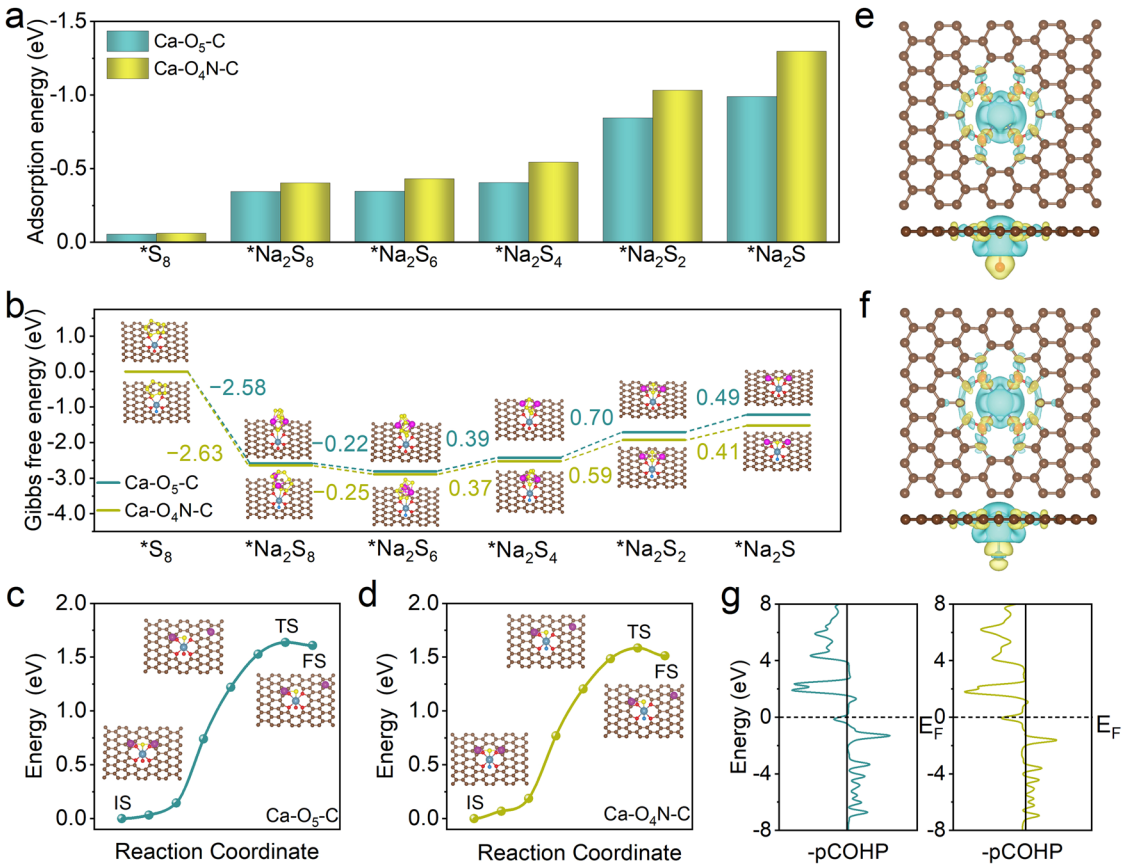

Fig. 6 | Theoretical calculations. a Adsorption energies of S_8 and Na_2S_n on Ca-O_5-C and Ca-O_4N-C. **b** Energy profiles for the reduction of S_8 and Na_2S_n on Ca-O_5-C and Ca-O_4N-C, and the corresponding interaction configurations. Energy profiles of the decomposition of Na_2S on **c** Ca-O_5-C and **d** Ca-O_4N-C. The charge density differences of **e** Ca-O_5-C and **f** Ca-O_4N-C from top view (up) and side view (down), the yellow color and cyan color represent the charge accumulation and depletion, respectively. **g** The -pCOHP curves for Na_2S_6 adsorption on Ca-O_5-C (left) and Ca-O_4N-C (right), the E_F denotes the Fermi level.

of Na_2S_6 adsorption on Ca-O_5-C and Ca-O_4N-C were −0.34 and −0.50, respectively, suggesting a stronger bonding interaction between Na_2S and Ca-O_4N-C. The above DFT calculations demonstrated that strong *p-p* orbital-hybridization between Ca atom and sulfur atom endowed the Ca-O_4N-C with a stronger affinity for Na_2S_n species, thus decreasing reaction barrier of Na−S batteries during the discharge/charge processes, thereby promoting the conversion kinetics of Na−S batteries.

In summary, we have successfully designed efficient s-block Ca SACs coordinated with one axial N atom and four planar O atoms dispersed on carbon nanosheets for efficient Na−S batteries. The axial N atom induces the localized electron distribution on the planar Ca−O_4 single-atom center to strengthen p-p orbital-hybridization of Ca SACs and Na_2S_n, which boosts the affinity toward Na_2S_n and simultaneously promotes the conversion kinetics of Na-S batteries. The Ca-O_4N-C@S exhibits superior sulfur conversion activity with a capacity of 1211 mAh g^{-1} at 0.2 C after 100 cycles, which outperforms most *d*-block SACs for Na−S batteries. Furthermore, Ca-O_4N-C@S exhibits long-term cyclic stability with a capacity of 887 mAh g^{-1} at 3.0 C after 800 cycles. This work offers a promising guidance for the design of efficient *s*-block metal SACs for Na-S batteries.

Methods

Chemicals

Calcium chloride ($CaCl_2$, 97%), propylene carbonate (PC, 99%) and fluoroethylene carbonate (FEC, 98%) were purchased from Shanghai Macklin Biochemical Co., Ltd. Carboxymethyl cellulose (CMC, 99%), and Super P were purchased from Guangdong Canrd New Energy Technology Co., Ltd. Sodium bis(trifluoromethylsulfonyl)imide (NaTFSI) were purchased from Changde Dado New Material Co., Ltd. Trimesic acid (BTC, 99%) was purchased from J&K Scientific Ltd. Metallic Na, *N,N*-dimethylformamide (DMF, 99.5%), hydrochloric acid (HCl, 38%), nitric acid (HNO_3, 68%) and sulfur were purchased from Sinopharm Chemical Reagent Co., Ltd.

Synthesis of Ca-BTC

Typically, 226 mg of trimesic acid and 83 mg of calcium chloride were dispersed in 40 mL of *N,N*-dimethylformamide (DMF) and refluxed at 180 °C for 2 h. The precipitate was washed by centrifuging with DMF three times, and dried at 60 °C in an oven overnight.

Synthesis of Ca-O_5-C

Ca-BTC was annealed at 600 °C for 2 h in N_2 and then etched with HCl for 30 min. The precipitate was further annealed at 800 °C for 2 h in N_2. The heating rate is 10 °C min^{-1}.

Synthesis of Ca-O_4N-C

Ca-BTC was annealed at 600 °C for 2 h in N_2 and then etched with HCl for 30 min. The precipitate was further annealed at 800 °C for 2 h in NH_3. The heating rate is 10 °C min^{-1}.

Synthesis of NCs

The synthesized procedures are similar with that for Ca-O_4N-C except for the acid ecthing by mixed acidic solution (HCl:HNO_3 = 3:1) for 12 h.

Synthesis of Ca-O_4N-C@S, Ca-O_5-C@S, NCs@S

For the synthesis of sulfur cathode, the sulfur host and sulfur were well mixed in mortar with a mass ratio of 1:2 (50 mg:100 mg). The mixtures

were heated at 155 °C for 12 h and then at 300 °C for 20 min in N_2 to obtain the Ca-O_4N-C@S, Ca-O_5-C@S, and NCs@S.

Materials characterization

X-ray diffraction (XRD, SmartLab 9KW) was conducted to confirm the phase of all samples. The morphologies of all samples were observed by scanning electron microscopy (SEM, JSM-6700 M), transmission electron microscopy (TEM, Hitachi H-800), and high-resolution TEM (HRTEM, JEOL-2011). The thermal stability was performed on a TGA-5500 thermoanalyser (TGA). The valence and composition of samples were investigated by X-ray photoelectron spectroscopy (XPS, ESCALAB 250 Xi). The specific surface area and pore characteristics were measured by a sorption analyzer (Micromeritics ASAP 2020) at 77 K. The soft XAS spectra were measured at the soft X-ray magnetic circular dichroism end station (XMCD) of the National Synchrotron Radiation Laboratory (NSRL) in the University of Science and Technology of China (USTC).

Electrochemical characterization

The as-prepared samples (Ca-O_4N-C@S, Ca-O_5-C@S, and NCs@S) were measured as cathodes to assemble a CR2032 coin-type cell in an argon-filled glove box (MBRAUN UNILAB PRO, SP (1800/780)). A slurry of active materials (70%), carboxymethyl cellulose (CMC) binder (10%), and Super P (20%), mixed in water with a mortar, was coated on the Al foil and dried in a vacuum oven at 60 °C overnight. The thickness and diameter are 150 μm and 14 mm, respectively. The mass loading of an electrode is about 1.0 mg cm^{-2}. The glass fiber (GF/D, Whatman, thickness: 660 μm, diameter: 18 mm) was used as a separator and metallic Na (thickness: 300 μm, diameter: 15 mm) was used as the counter electrode with 2 M sodium bis(trifluoromethylsulfonyl)imide (NaTFSI) in propylene carbonate/fluoroethylene carbonate (PC/FEC, 1/1 by volume) as an electrolye. An electrolyte-to-sulfur ratio is 70 μL mg^{-1}. The surface oxide layer of Na was removed with a knife. The 2032-type coin cells were assembled in an Ar-filled glove box (H_2O <0.1 ppm, O_2 <0.1 ppm). The capacity and cycling performances were tested between 0.5 and 2.8 V on a battery testing system (Neware). Cyclic voltammetry (CV) measurements (0.5–2.8 V vs. Na^+/Na) and Electrochemical impedance spectroscopy (EIS) tests (amplitude: 5 mV, frequency from 100 kHz to 0.01 Hz) were performed on a CHI760E electrochemical workstation. The data used for Tafel analysis was derived from the CV curves. All electrochemical tests were performed at 25 °C in an environmental chamber. The capacity values are calculated based on the mass of sulfur in cathodes.

Synthesis of Na_2S_6 solution

The Na_2S_6 solution was obtained through adding sulfur and Na_2S powder with the molar ratio of 5:1 in a mixed solution of PC and FEC (1:1 by volume), and then continuously stirred at 80 °C for 24 h in the argon-filled glove box. The Na_2S_6 solution with the atomic sulfur concentration of 0.2 M was obtained.

Na_2S_6 solution adsorption experiment

The Ca-O_4N-C, Ca-O_5-C, and NCs with the same mass of 2 mg were added into the diluted Na_2S_6 solution (2 mL), respectively. The adsoption experiment was performed in an argon-filled glove box. The adsorption ability was measured by ultraviolet-visible (UV–vis) spectroscopy after the active materials soaked in the Na_2S_6 solution for 12 h.

Na_2S precipitation experiments

The Na_2S precipitation experiments were tested with CR2032-type coin cells on the gamry workstation. A slurry of samples (70%, Ca-O_4N-C, Ca-O_5-C, and NCs), carboxymethyl cellulose (CMC) binder (10%), and Super P (20%), mixed in water, was coated on carbon paper and dried in a vacuum oven at 60 °C for 12 h. A GF/D membrane was used as the separator and Na was used as the anode. About 45 μL of Na_2S_6 solution as electrolyte was added on the cathode side and 75 μL of PC/FEC (1/1 by volume) solvent was dropped on the anode side. The cell was first galvanostatically discharged to 1.3 V and then kept at a voltage of 1.2 V until the current was below 10^{-9} A.

Theoretical computation

All calculations were carried out using the Vienna Ab initio Simulation Package (VASP) based on the density functional theory (DFT)[61]. The projector augmented wave (PAW) method was used to describe electron–ion interactions. The gradient-corrected Perdew–Burke–Ernzerh (GGA-PBE) functional was adopted to describe electron exchange and correlation energy[62]. The cutoff energy was set to 400 eV. The convergence of total energy and forces was set to 1×10^{-5} eV and 0.01 eV/Å, respectively. A Monkhorst-Pack $3 \times 3 \times 1$ k-point grid was used to sample the Brillouin zon[63]. To guarantee full relaxation, 15 Å vacuum space was introduced in the z-direction. The activation energy for Na_2S decomposition was calculated with the climbing-image nudged elastic band (CI–NEB) method[55]. The projected crystal orbital Hamilton population (pCOHP) was employed to reveal the nature of bonding between Ca SACs and Na_2S_n intermediates[58–60]. The ab initio molecular dynamics (AIMD) simulations were performed in the canonical ensemble (NVT) with constant temperature in the Nosé-Hoover heat bath at 300 K for 10 ps[64]. During the simulations, the Brillouin-zone samplings adopt a Γ-point grid. The initial velocities of ions were randomly assigned by Maxwell–Boltzmann distribution at the targeting temperature. The time step was set to be 3 fs.

The adsorption energies of S_8 and Na_2S_n (n = 8, 6, 4, 2, 1) species on NCs and Ca-SACs, were defined as:

$$\Delta E = E_{total} - E_{sub} - E_{species} \quad (1)$$

where E_{total} was the total energy of S_8 or Na_2S_n species on NCs and Ca-SACs, E_{sub} was the energy of the clean substrate, $E_{species}$ was the energy of S_8 or Na_2S_n (n = 8, 6, 4, 2, 1) species.

The Gibbs free energy reaction profile of S_8 and Na_2S_n (n = 8, 6, 4, 2, 1) species on NCs and Ca-SACs could be calculated as follows:

$$\Delta G = \Delta E + \Delta ZPE - T\Delta S \quad (2)$$

where ΔE was the adsorption energy of S_8 or Na_2S_n (n = 8, 6, 4, 2, 1) species on NCs or Ca-SACs, ΔZPE was the change in zero-point energy, T was the temperature (298.15 K), and ΔS was the change in entropy.

The decomposition processes of Na_2S on Ca-O_5-C and Ca-O_4N-C were calculated as follows:

$$*Na_2S \rightarrow *NaS + Na^+ + e^- \quad (3)$$

in which * represents Ca-O_5-C or Ca-O_4N-C.

The binding energies of an isolated sulfur atom on Ca-O_5-C and Ca-O_4N-C was calculated using the following equation:

$$E_b = E_{S*} - E* - E_S \quad (4)$$

where E_{S*} is the total energy of a Ca single-atom catalyst with a bonded isolate sulfur atom, $E*$ is the energy of Ca single-atom catalyst, E_S denotes the energy of isolate sulfur atom.

Data availability

The data generated in this study are available within the main text and the Supplemental Information. Source data are provided with this paper.

References

1. Wei, Z. Y. et al. Establishing reaction networks in the 16-electron sulfur reduction reaction. *Nature* **626**, 98–104 (2024).
2. Hua, W. X. et al. Optimizing the p charge of S in p-block metal sulfides for sulfur reduction electrocatalysis. *Nat. Catal.* **6**, 174–184 (2023).
3. Wang, L. et al. The promises, challenges and pathways to room-temperature sodium-sulfur batteries. *Nat. Sci. Rev.* **9**, nwab050 (2022).
4. Wang, J. Y. et al. Coordinatively deficient single-atom Fe-N-C electrocatalyst with optimized electronic structure for high-performance lithium-sulfur batteries. *Energy Storage Mater* **46**, 269–277 (2022).
5. Eng, A. Y. S. et al. Room-temperature sodium-sulfur batteries and beyond: realizing practical high energy systems through anode, cathode, and electrolyte engineering. *Adv. Energy Mater.* **11**, 2003493 (2021).
6. Aslam, M. K. et al. Metal chalcogenide hollow polar bipyramid prisms as efficient sulfur hosts for Na-S batteries. *Nat. Commun.* **11**, 5242 (2020).
7. Wu, S. C. et al. Rational design of a polysulfide catholyte electrocatalyst by interfacial engineering based on novel MoS_2/MoN heterostructures for superior room-temperature Na-S batteries. *Nano Energy* **90**, 106590 (2021).
8. Zhou, X. F. et al. A high-efficiency Mo_2C electrocatalyst promoting the polysulfide redox kinetics for Na-S batteries. *Adv. Mater.* **34**, 2200479 (2022).
9. Ding, Y. F. et al. Enhanced dual-directional sulfur redox via a biotemplated single-atomic Fe-N_2 mediator promises durable Li-S batteries. *Adv. Mater.* **34**, 2202256 (2022).
10. Bai, R. L. et al. Toward complete transformation of sodium polysulfides by regulating the second-shell coordinating environment of atomically dispersed Fe. *Angew. Chem. Int. Ed.* **62**, e202218165 (2023).
11. Li, Z. et al. Room-temperature sodium-sulfur batteries: rules for catalyst selection and electrode design. *Adv. Mater.* **34**, 2204214 (2022).
12. Zhang, E. H. et al. Single-atom yttrium engineering janus electrode for rechargeable Na-S batteries. *J. Am. Chem. Soc.* **144**, 18995–19007 (2022).
13. Sun, T. T. et al. Strengthened d-p orbital-hybridization of single atoms with sulfur species induced bidirectional catalysis for lithium-sulfur batteries. *Adv. Funct. Mater.* **33**, 2306049 (2023).
14. Jiang, Y. et al. Single-atom vanadium catalyst boosting reaction kinetics of polysulfides in Na-S batteries. *Adv. Mater.* **35**, 2208873 (2023).
15. Huang, X. L., Wang, Y. X., Chou, S. L., Dou, S. X. & Wang, Z. M. Materials engineering for adsorption and catalysis in room-temperature Na-S batteries. *Energy Environ. Sci.* **14**, 3757–3795 (2021).
16. Zhu, R. et al. Modulating bond interactions and interface microenvironments between polysulfide and catalysts toward advanced metal-sulfur batteries. *Adv. Funct. Mater.* **32**, 2207021 (2022).
17. Zhang, B. W. et al. Atomic cobalt as an efficient electrocatalyst in sulfur cathodes for superior room-temperature sodium-sulfur batteries. *Nat. Commun.* **9**, 4082 (2018).
18. Fang, D. L. et al. An exfoliation-evaporation strategy to regulate N coordination number of Co single-atom catalysts for high-performance lithium-sulfur batteries. *ACS Mater. Lett.* **4**, 1–10 (2022).
19. Wang, Y. Z. et al. Manipulation of edge-site Fe-N_2 moiety on holey Fe,N codoped graphene to promote the cycle stability and rate Capacity of Li-S batteries. *Adv. Funct. Mater.* **29**, 1807485 (2019).
20. Wang, Y. et al. Phosphor-doped carbon network electrocatalyst enables accelerated redox kinetics of polysulfides for sodium-sulfur batteries. *ACS Nano* **18**, 3839–3849 (2024).
21. Ye, C. et al. A Mo_5N_6 electrocatalyst for efficient Na_2S electrodeposition in room-temperature sodium-sulfur batteries. *Nat. Commun.* **12**, 7195 (2021).
22. Xiao, F. P. et al. Generating short-chain sulfur suitable for efficient sodium-sulfur batteries via atomic copper sites on a N,O-codoped carbon composite. *Adv. Energy Mater.* **11**, 2100989 (2021).
23. Gu, Y., Xi, B. J., Zhang, H., Ma, Y. C. & Xiong, S. L. Activation of main-group antimony atomic sites for oxygen reduction catalysis. *Angew. Chem.* **134**, e202202200 (2022).
24. Yao, G. et al. Highly flexible carbon film implanted with single-atomic Zn–N_2 moiety for long-life sodium-sulfur batterie. *Adv. Funct. Mater.* **34**, 2214353 (2024).
25. Qiu, Y. et al. Precise synthesis of Fe-N_2 sites with high activity and stability for long-life lithium-sulfur batteries. *ACS Nano* **14**, 16105–16113 (2020).
26. Sun, X. et al. Isolated Fe-Co heteronuclear diatomic sites as efficient bifunctional catalysts for high performance lithium-sulfur batteries. *Nat. Commun.* **14**, 291 (2023).
27. Liu, Y. N. et al. O-, N-coordinated single Mn atoms accelerating polysulfides transformation in lithium-sulfur batteries. *Energy Storage Mater* **35**, 12–18 (2021).
28. Xiao, C. X. et al. P-block tin single atom catalyst for improved electrochemistry in a lithium-sulfur battery: a theoretical and experimental study. *J. Mater. Chem. A* **10**, 3667–3677 (2022).
29. Liu, S. et al. Turning main-group element magnesium into a highly active electrocatalyst for oxygen reduction reaction. *Nat. Commun.* **11**, 938 (2020).
30. Wang, Q. Y. et al. Asymmetric coordination induces electron localization at Ca sites for robust CO_2 electroreduction to CO. *Adv. Mater.* **35**, 2300695 (2023).
31. Lin, Z. Y. et al. Tuning the p-orbital electron structure of s-block metal Ca enables a high-performance electrocatalyst for oxygen reduction. *Adv. Mater.* **33**, 2107103 (2021).
32. Zheng, F. C. et al. Pentagon defects accelerating polysulfides conversion enabled high-performance sodium-sulfur batteries. *Adv. Funct. Mater.* **34**, 2310598 (2024).
33. Yang, Y. et al. O-, N-atoms-coordinated Mn cofactors within a graphene framework as bioinspired oxygen reduction reaction electrocatalysts. *Adv. Mater.* **30**, 1801732 (2018).
34. Zhao, C. M. et al. Solid-diffusion synthesis of single-atom catalysts directly from bulk metal for efficient CO_2 reduction. *Joule* **3**, 584–594 (2019).
35. Zhang, C. et al. A pentagonal defect-rich metal-free carbon electrocatalyst for boosting acidic O_2 reduction to H_2O_2 production. *J. Am. Chem. Soc.* **145**, 11589–11598 (2023).
36. Deng, Y. C. et al. Operando spectroscopic analysis of axial oxygen-coordinated single-Sn-atom sites for electrochemical CO_2 reduction. *J. Am. Chem. Soc.* **145**, 7242–7251 (2023).
37. Zhang, Y. G. et al. Engineering oversaturated Fe-N_5 multifunctional catalytic sites for durable lithium-sulfur batteries. *Angew. Chem. Int. Ed.* **60**, 26622–26629 (2021).
38. Sun, T. T. et al. $NiMoO_4$ nanosheets anchored on N-S doped carbon clothes with hierarchical structure as a bidirectional catalyst toward accelerating polysulfides conversion for Li-S battery. *Adv. Funct. Mater.* **31**, 2101285 (2021).
39. Fang, D. L. et al. Core–shell tandem catalysis coupled with interface engineering for high-performance room-temperature Na–S batteries. *Small* **19**, 2302461 (2023).
40. Ma, C. S. et al. Dynamic multistage coupling of FeS_2/S enables ultrahigh reversible Na-S batteries. *Adv. Funct. Mater.* **33**, 2211821 (2023).
41. Wang, L. F. et al. Manipulating the electronic structure of nickel via alloying with iron: toward high-kinetics sulfur cathode for Na-S batteries. *ACS Nano* **15**, 15218–15228 (2021).

42. Guo, Q. B. et al. Ultrastable sodium-sulfur batteries without polysulfides formation using slit ultramicropore carbon carrier. *Adv. Sci.* **7**, 1903246 (2020).
43. Huang, Z. P. et al. High-capacity and stable sodium-sulfur battery enabled by confined electrocatalytic polysulfides full conversion. *Adv. Funct. Mater.* **31**, 2100666 (2021).
44. Wu, C. et al. Continuous carbon channels enable full Na-ion accessibility for superior room-temperature Na-S batteries. *Adv. Mater.* **34**, 2108386 (2022).
45. Xiao, F. P. et al. Covalent encapsulation of sulfur in a MOF-derived S, N-doped porous carbon host realized via the vapor-infiltration method results in enhanced sodium–sulfur battery performance. *Adv. Energy Mater.* **10**, 2000931 (2020).
46. Zhang, S. P. et al. Mo_2N-W_2N heterostructures embedded in spherical carbon superstructure as highly efficient polysulfide electrocatalysts for stable room-temperature Na-S batteries. *Adv. Mater.* **33**, 2103846 (2021).
47. Qin, G. et al. High performance room temperature Na-S batteries based on FCNT modified Co_3C-Co nanocubes. *Chem. Eng. J.* **396**, 125295 (2020).
48. Chen, S. F. et al. Brain capillary-inspired self-assembled covalent organic framework membrane for sodium–sulfur battery separator. *Adv. Energy Mater.* **13**, 2204334 (2023).
49. Zhang, B. W. et al. Atomically dispersed dual-site cathode with a record high sulfur mass loading for high-performance room-temperature sodium-sulfur batteries. *Adv. Mater.* **5**, 2206828 (2023).
50. Yang, H. L. et al. Architecting freestanding sulfur cathodes for superior room-temperature Na–S batteries. *Adv. Funct. Mater.* **31**, 2102280 (2021).
51. Zhang, H. et al. Bidirectional tandem electrocatalysis manipulated sulfur speciation pathway for high-capacity and stable Na-S battery. *Angew. Chem. Int. Ed.* **62**, e202217009 (2023).
52. Weng, S. X. et al. Unraveling the multifunctional mechanism of fluoroethylene carbonate in enhancing high-performance room-temperature sodium-sulfur batteries. *Angew. Chem. Int. Ed.* **64**, e202217009 (2024).
53. Jayan, J. & Islam, M. M. Design principles of bifunctional electrocatalysts for engineering interfaces in Na–S batteries. *ACS Catal.* **11**, 15149–15161 (2021).
54. Qiang, Z. et al. Ultra-long cycle life, low-cost room temperature sodium–sulfur batteries enabled by highly doped (N,S) nanoporous carbons. *Nano Energy* **32**, 59–66 (2017).
55. Henkelman, G., Uberuaga, B. P. & Jónsson, H. A climbing image nudged elastic band method for finding saddle points and minimum energy paths. *J. Chem. Phys.* **113**, 9901–9904 (2000).
56. Song, X. Q. et al. Improving poisoning resistance of electrocatalysts via alloying strategy for high-performance lithium-sulfur batteries. *Energy Storage Mater* **41**, 248–254 (2021).
57. Shou, Y. Q. et al. Achieving highly reversible all-solid-state lithium-sulfur batteries through metal–sulfur bonding regulation. *ACS Mater. Lett.* **6**, 4545–4554 (2024).
58. Dronskowski, R. & Bloechl, P. E. Crystal orbital Hamilton populations (COHP): energy-resolved visualization of chemical bonding in solids based on density-functional calculations. *J. Phys. Chem.* **97**, 8617–8624 (1993).
59. Deringer, V. L., Tchougréeff, A. L. & Dronskowski, R. Crystal orbital hamilton population (COHP) analysis as projected from plane-wave basis sets. *J. Phys. Chem. A.* **115**, 5461–5466 (2011).
60. Maintz, S., Deringer, V. L., Tchougréeff, A. L. & Dronskowski, R. LOBSTER: a tool to extract chemical bonding from plane-wave based DFT. *J. Comput. Chem.* **37**, 1030–1035 (2016).
61. Kresse, G. & Hafner, J. Ab-initio molecular-dynamics for open-shell transition-metals. *Phys. Rev. B* **48**, 13115–13118 (1993).
62. Perdew, J. P., Burke, K. & Ernzerhof, M. Generalized gradient approximation made simple. *Phys. Rev. Lett.* **77**, 3865–3868 (1996).
63. Monkhorst, H. J. & Pack, J. D. Special points for Brillouin-zone integrations. *Phys. Rev. B.* **13**, 5188–5192 (1976).
64. Hoover, W. G. Canonical dynamics: equilibrium phase-space distributions. *Phys. Rev. A* **31**, 1695–1697 (1985).

Acknowledgements

We gratefully acknowledge the financial support from the National Key R&D Program of China (Grant No. 2021YFA1600202), National Natural Science Foundation of China (U2032162 and 52302159), and China Postdoctoral Science Foundation (2023M740003). Supercomputing Center of the University of Science and Technology of China for computational support.

Author contributions

F.Z., Y.Z., and H.W. designed and carried out research, analyzed data, and wrote the paper. C.W. contributed to the theoretical calculation in this paper. Z.L. and G.Y. contributed to write the paper. L.W. helped with the structural characterizations. Q.C. supervised the project.

Competing interests

The authors declare no competing interests.

Additional information

Supplementary information The online version contains supplementary material available at https://doi.org/10.1038/s41467-025-59437-3.

Correspondence and requests for materials should be addressed to Changlai Wang or Hui Wang.

Peer review information *Nature Communications* thanks Md Mahbubul Islam, and the other, anonymous, reviewers for their contribution to the peer review of this work. A peer review file is available.